ADVANCED MATERIALS

www.advmat.de

Textile Inspired Lithium–Oxygen Battery Cathode with Decoupled Oxygen and Electrolyte Pathways

Shaomao Xu, Yonggang Yao, Yuanyuan Guo, Xiaoqiao Zeng, Steven D. Lacey, Huiyu Song, Chaoji Chen, Yiju Li, Jiaqi Dai, Yanbin Wang, Yanan Chen, Boyang Liu, Kun Fu, Khalil Amine, Jun Lu, and Liangbing Hu**

The lithium–air ($Li–O_2$) battery has been deemed one of the most promising next-generation energy-storage devices due to its ultrahigh energy density. However, in conventional porous carbon–air cathodes, the oxygen gas and electrolyte often compete for transport pathways, which limit battery performance. Here, a novel textile-based air cathode is developed with a triple-phase structure to improve overall battery performance. The hierarchical structure of the conductive textile network leads to decoupled pathways for oxygen gas and electrolyte: oxygen flows through the woven mesh while the electrolyte diffuses along the textile fibers. Due to noncompetitive transport, the textile-based $Li–O_2$ cathode exhibits a high discharge capacity of 8.6 mAh cm^{-2}, a low overpotential of 1.15 V, and stable operation exceeding 50 cycles. The textile-based structure can be applied to a range of applications (fuel cells, water splitting, and redox flow batteries) that involve multiple phase reactions. The reported decoupled transport pathway design also spurs potential toward flexible/wearable $Li–O_2$ batteries.

The search for high-energy-density energy-storage systems has been a high priority due to the growing demand for energy and the gradual depletion of conventional fossil fuels. Since its invention in 1996,[1] the lithium–air battery, with a theoretical energy density of 3500 Wh kg^{-1}, has been widely considered one of the most promising energy-storage systems.[2–6] However, there are many obstacles impeding the application of the lithium–air battery including a high charge–discharge overpotential introduced by the insulating discharge product,[7,8] instability between the electrolyte and electrodes,[9,10] and side reactions caused by ambient air impurities.[11,12] Numerous research efforts have been devoted to improve lithium–air battery performance: (1) instead of conventional organic electrolytes, solid state and hybrid electrolytes have been employed to prevent attack via O_2 radicals;[13–16] (2) more stable cathode materials have been utilized to reduce/avoid side reactions associated with electrode decomposition;[17–20] active heterogeneous catalysts have been introduced to improve the kinetics of the oxygen reduction reaction (ORR) and oxygen evolution reaction (OER) during the discharge and charge processes, respectively;[21,22] redox mediators have enabled a solution-based reaction mechanism to resolve the insulating nature of the discharge products;[23–26] the effect of moisture and carbon dioxide have been studied to realize a true lithium "ambient air" battery.[27–30]

To date, most lithium–air battery studies employ organic electrolytes and pure oxygen as the cathode gas, which cause complicated reactions (i.e., oxygen dissolution/evolution at the oxygen–electrolyte interface and ORR/OER at the cathode–electrolyte interface) to occur on the cathode surface. Hence, the structure of the cathode plays a crucial role in the overall performance of the lithium–air battery. Recent studies have shown that increasing the gas permeability of the cathode leads to increased capacity and rechargeability of the battery.[31] However, in conventional lithium–air cathodes, the transport of both electrolyte and oxygen gas occurs within the porous sections of the carbon framework, which may lead to unutilized active sites on the cathode. Specifically, some cathode sections possess excess electrolyte with limited oxygen gas flow, while other oxygen-rich areas repel the electrolyte. In both situations, the cathode active sites lack a critical component (O_2 or electrolyte), which leads to capacity loss due to underutilized reactions. These mass transport limitations remain unsolved and present a fundamental challenge for lithium–air batteries.

In this study, we developed a novel triple-phase structure using a flexible textile-based lithium–air battery cathode. The woven textile-based air cathode has an inherently open structure and enables separate transport pathways for the electrolyte and oxygen gas: the electrolyte transfers along the textile fibers while the oxygen gas can diffuse through the woven mesh holes. Due to this noncompetitive transport design, the entirety of the air cathode is accessible to both electrolyte and

Dr. S. Xu, Y. Yao, S. D. Lacey, Prof. H. Song, Dr. C. Chen, Y. Li, J. Dai, Y. Wang, Dr. Y. Chen, B. Liu, Dr. K. Fu, Prof. L. Hu
Department of Materials Science and Engineering
University of Maryland College Park
College Park, MD 20742, USA
E-mail: binghu@umd.edu

Dr. Y. Guo, Dr. X. Zeng, Dr. K. Amine, Dr. J. Lu
Chemical Sciences and Engineering Division
Argonne National Laboratory
Argonne, IL 60439, USA
E-mail: junlu@anl.gov

The ORCID identification number(s) for the author(s) of this article can be found under https://doi.org/10.1002/adma.201704907.

DOI: 10.1002/adma.201704907

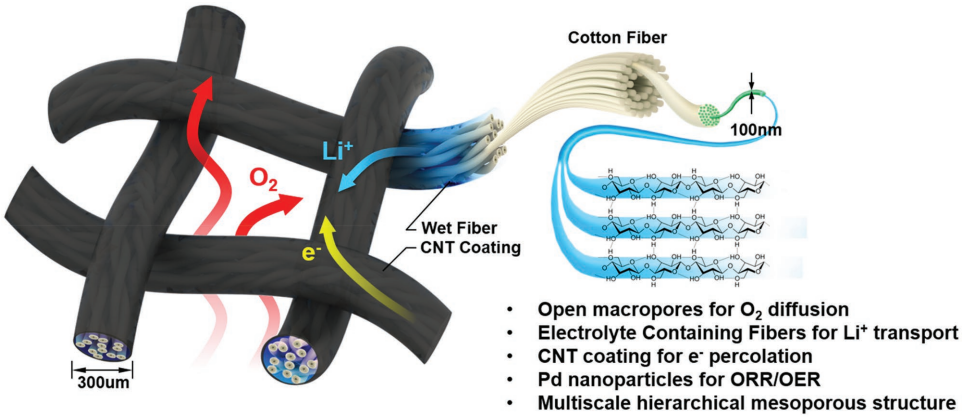

Figure 1. Schematic representation of the design and decoupled pathways (O_2 gas, electrolyte) within the wet textile-based air cathode. The structure of the air cathode facilitates mass and ionic transport: O_2 gas flows through the woven mesh, fast Li^+ transport along the textile fibers, and rapid electron transfer along the CNT-coated textile surface. The coated textile, composed of intertwined nanofibers and microchannels, acts as a nanoionic device by facilitating both electrolyte and ionic (Li^+) transport.

oxygen gas. With full utilization of active sites, the textile-based air cathode demonstrates exceptional electrochemical performance: a full discharge capacity of 8.6 mAh cm^{-2}, an overall overpotential below 1.15 V, and stable cyclability (>50 cycles) with complete decomposition of the discharge product. The decoupled electrolyte and oxygen gas pathways in the textile-based structure promote a new direction of lithium–air cathode design beyond increasing surface area and controlling pore size. Additionally, the textile-based cathode design can be potentially used for flexible, even wearable battery design.[32,33] Note that lithium–air battery does not have active materials in the cathode, which is natural advantage to be engineered into a flexible device without the problems of delamination and loss of cathode materials.[34–38]

The concept of the ari-breathable-textile-based Li–O_2 cathode is shown in **Figure 1**. From a macroscale standpoint, the textile air cathode is a mesh structure of intertwined fibers with a conductive surface layer of carbon nanotubes (CNT). The CNT layer forms an electron conductive pathway while the hierarchical structure of the textile enables channels for electrolyte to flow through. Note that the raw textile fabric has a good affinity with the liquid electrolyte. Therefore, the electrolyte flows underneath the active sites on the CNT coating layer to promote the reaction processes. The size of the textile mesh holes is more than sufficient for oxygen transport, which is essential to facilitate the ORR process during discharge.[31] In this case, the liquid electrolyte and the flow of oxygen gas occurs on opposite sides of the active CNT coating layer, which enables decoupled pathways and full utilization of active sites on the CNT layer for enhanced Li–O_2 battery performance. On the microscale, the CNTs are decorated with 10 nm palladium (Pd) catalyst nanoparticles. Similar to the active CNT layer, the Pd nanocatalysts are exposed to both electrolyte and oxygen gas to ensure full catalyst functionality. This unique textile triple-phase structure provides an excellent cathode design platform for lithium–air batteries.

The flexibility and morphology of the textile-based air cathode is illustrated in **Figure 2**. Solution-based processes were used to fabricate the flexible textile-based air cathode. First, the raw textile fabric was repeatedly coated with a 10 mg mL^{-1} CNT ink to ensure uniform CNT deposition. Next, the CNT-coated textile was dipped in a $PdCl_2$ solution to load the catalyst precursor. Finally, Pd nanoparticles were created by chemical reduction with an $NaBH_4$ solution to obtain the reported air cathode. Figure 2a illustrates the flexibility of the textile-based air cathode through bend, fold, and twist tests. In this case, the flexibility of the raw textile fabric was maintained after the aforementioned fabrication process. The textile-based air cathode is highly bendable and twistable and exhibits remarkable mechanical strength. Even after 50 cycles of bending and twisting, the air cathode recovers to its original shape (Figure S1, Supporting Information). Therefore, the reported textile-based cathode structure can be envisioned as a flexible and wearable Li–O_2 battery.

Confocal microscopy and scanning electron microscopy (SEM) were employed to study the morphology of the textile-based air cathode (Figure 2b–f). Figure 2b shows the macroscale textile structure with an even distribution of intertwined cotton and polyester threads and 100 µm square holes. Fibers with 10–20 µm diameters are knitted together to form the woven mesh network, as shown by low magnification SEM (Figure 2c). Each individual fiber has a rough surface due to the CNT dip coating procedure (Figure 2d). Figure 2e shows the cotton fiber microchannels below the CNT coating layer in the textile-based air cathode. Note that these cotton fiber microchannels are stabilized by the surrounding polyester fibers and act as a nanoionic material by facilitating ion and electrolyte transport. High-magnification SEM revealed CNTs with 10 nm diameters densely covering the textile fibers (Figure 2f). High-resolution transmission electron microscopy (TEM) reveals that the 2–5 nm Pd nanoparticles uniformly decorate the CNT network (Figure S2, Supporting Information). These unique structural and morphological features of the textile-based cathode are promising indicators for high-performance lithium–air batteries.

The mass and ionic transport properties of the air cathode are essential for battery performance. Specifically, reactions at the air cathode involve oxygen gas, lithium ions that pass through the liquid electrolyte and electrons that transport

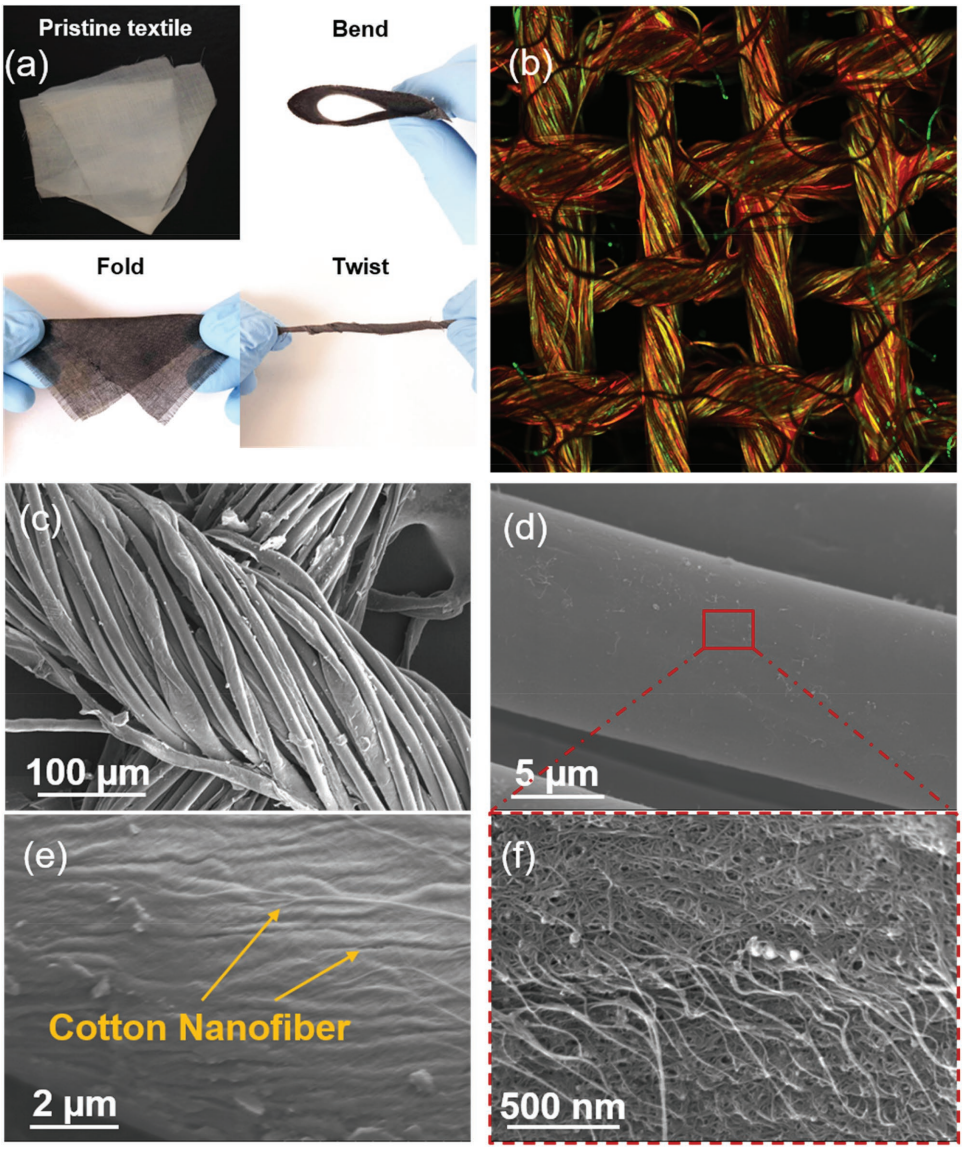

Figure 2. The flexibility and morphology of the textile-based air cathode. a) Digital images of the raw textile fabric and the textile-based air cathode. The CNT- and Pd catalyst-loaded textile exhibits excellent flexibility through bend, fold, and twist tests. b) A confocal microscopy image showing an even distribution of cotton (red) and polyester (green) textile components. The macroscale textile mesh possesses 100 µm holes for facile oxygen transport throughout the air cathode. c,d) SEM images showing the hierarchical fiber network (c), as well as a single textile fiber within the textile-based air cathode (d). The rough fiber surface indicates a dense CNT coating. e) SEM image of the textile below the CNT coating composed of cotton nanofibers surrounded by polyester fibers. f) High-magnification SEM image showing the conformal CNT-coating layer as well as the Pd nanocatalysts that decorate the textile cathode.

along the CNTs coating the textile surface. Therefore, the gas permeability, Li^+ ion conductivity, and electron conductivity of the textile-based air cathode were studied in depth (**Figure 3**). The transport properties for both the full textile (Figure 3a) and a single fiber (Figure 3b) has been studied. The gas permeability test elucidated the relationship between the gas flow rate through the cathode at a given applied pressure. Similar to an actual coin cell, electrolyte is applied to the cathode before testing. In this case, when electrolyte is added, the fiber diameter increases while the mesh hole size decreases. This causes the nanofibers within the textile threads to act as electrolyte flow channels; however, oxygen gas becomes hampered due to the swelling. Nevertheless, the textile-based cathode maintains a high gas flow rate of 650 mm s^{-1} under a pressure of 200 Pa, which is much higher than conventional Li–O_2 cathodes.[39,40] This result supports the decoupled oxygen and electrolyte pathways present within the textile-based triple-phase structure.

The electronic conductivity of the CNT-coated breathable textile was measured by the four probe method (Figure 3d). Schematic representations of both the full textile (Figure 3a) and a single fiber (Figure 3b) depict the types of electronic conductivity test samples. Based on the *I*–*V* curves, the single fiber exhibited a resistance of 1250 Ω and a conductivity of 50 S cm^{-1}, while the resistance and conductivity of the full

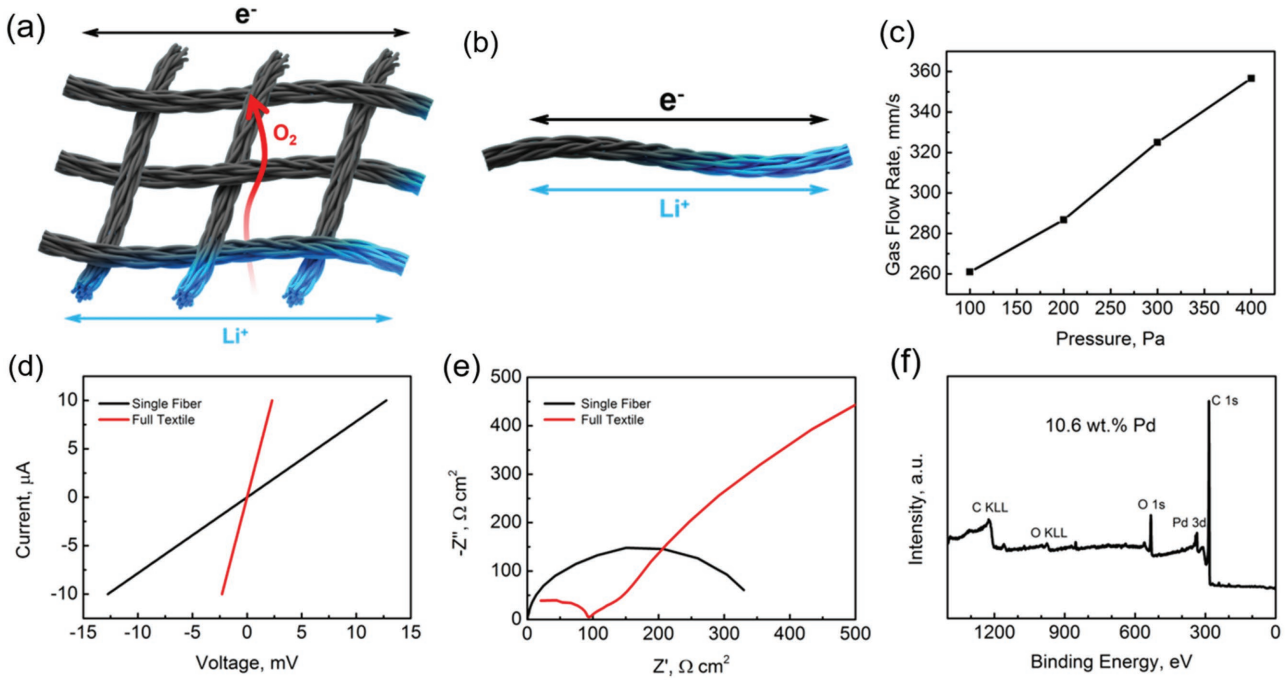

Figure 3. The transport properties of the textile-based air cathode. a) Schematic of the textile-based cathode. The oxygen gas can flow through the mesh holes while Li^+ and electrons can transport along the textile fibers. b) Schematic of a single textile fiber. Electrons transfer along the CNT surface while Li^+ transfer through the fiber microchannels. c) The gas permeability of the textile-based air cathode soaked with electrolyte. d) *I–V* curves (d) and EIS results (e) for both a single textile fiber and the full textile-based air cathode. f) XPS survey scan of the air cathode with a Pd loading of 10.6 wt%.

textile was 227 Ω and 125 S cm^{-1}, respectively. The higher conductivity of the full textile can be attributed to the interconnected CNT network. In this case, the conformal CNT coating connects multiple textile fibers together to provide facile electron transport pathways.

Electrochemical impedance spectroscopy (EIS) provided information regarding the lithium ion conductivity of the wet, breathable textile-based air cathode. Figure 3e shows the EIS curves for both a single fiber and the full textile-based cathode. In both cases, the resistance is on the order of a few hundred Ω cm^2, which corresponds to a conductivity of ≈10^{-3} S cm^{-1}. Note that this is the same conductivity value as the liquid electrolyte. The high ionic conductivity indicates that the textile fibers form highways for Li^+ ion diffusion that promote and retain the initial conductivity of the electrolyte. The single fiber has a lower ionic conductivity compared to the full textile, which is reasonable since the interconnected textile fibers facilitate enhanced Li^+ ion transport. The excellent gas permeability, electronic conductivity, and ionic conductivity of the textile-based air cathode ensure that transport does not become the limiting factor, which is key to improve Li–O_2 battery performance.

The OER and ORR kinetics are another key factor for Li–O_2 batteries. In the textile-based air cathode, the OER/ORR processes are catalyzed by Pd nanoparticles embedded in the CNT-coated network. The loading of the Pd nanoparticles (10.6 wt%) on the textile air cathode was determined by X-ray photoelectron spectroscopy (XPS). The survey scan of the CNT-coated air cathode shows both oxygen and carbon peaks as well as Pd 3d peaks around 335 eV (Figure 3f). Through detailed analysis of the Pd 3d peaks, both Pd metal and PdO were detected (Figure S3, Supporting Information). The existence of PdO is inevitable since even slight exposure to ambient air creates a thin oxide layer on the catalyst nanoparticles. Due to the open structure of the cathode, the nanocatalysts are fully exposed to the oxygen gas stream and electrolyte flow causing enhanced involvement toward ORR/OER processes. Therefore, the textile-based air cathode design is expected to improve electrochemical performance even though the Pd catalyst loading is low.

To illustrate the use of the wet and breathable textile as an air cathode, Li–O_2 batteries were assembled and fully discharged to 2 V at a current density of 0.1 mA cm^{-2}. The discharge profiles are shown in **Figure 4**a. When the cathode is not saturated with electrolyte, the mesh holes remain large enough to facilitate gas flow (Figure 4b). Therefore, the source of Li^+ ions and oxygen gas is maintained during the discharge process, which leads to a lower discharge overpotential and a discharge capacity of 8.6 mAh cm^{-2}. However, if the air cathode is flooded with excess electrolyte, the gas flow is partially blocked (Figure 4c). This hampers battery performance substantially and results in much higher discharge overpotential and a lower discharge capacity of 2.5 mAh cm^{-2}.

The significance of decoupled transport pathways was further studied via postmortem cell characterization. SEM images of the discharge products for both the breathable and flooded textile-based cathodes are shown in Figure 4d,e. If the air cathode has an optimal amount of electrolyte (i.e., the gas flow channels are not blocked), a thick layer of discharge products forms on the cathode surface after discharge. In this case, the CNT network is fully covered with clusters of discharge products, which indicates full utilization of cathode active sites to achieve a high discharge capacity. However, if the cathode is

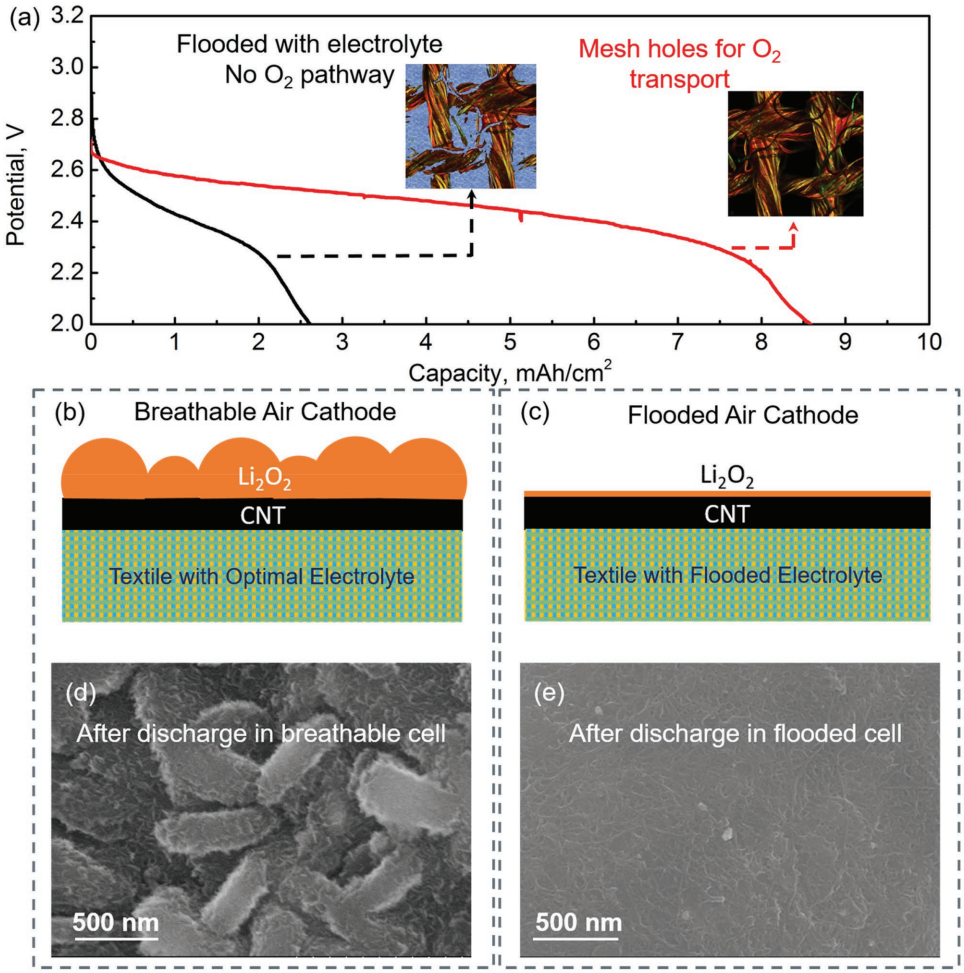

Figure 4. Discharge characteristics of the textile-based Li–O_2 battery cathode. a) Discharge profiles of cells with an optimal amount of electrolyte (breathable cathode) and excess electrolyte (flooded cathode as a control). Insets show the textile-based cathode structures for both cases, where the blue background indicates the overflow of electrolyte. b) Schematic of a breathable cathode with an optimal amount of electrolyte. The mesh holes facilitate facile oxygen transport, which leads to increased formation of discharge products and high discharge capacity. c) Schematic of a flooded air cathode. The oxygen gas flow is inhibited due to the excess electrolyte, which leads to the formation of a thin layer of discharge products and lower discharge capacity. d) SEM image of the breathable cathode in the discharge state. The entire cathode is covered by a thick layer of discharge products. e) SEM image of a flooded cathode in the discharge state. The CNT coating is visible with a small amount of discharge products on the cathode surface. Postmortem characterization of cathodes in the discharge state confirmed the importance of the breathable triple-phase structure.

flooded with excess electrolyte (i.e., the gas flow is inhibited), a thin layer of discharge products is formed on the cathode surface and the CNT coating is still observed. The lack of discharge product formation indicates that only a small portion of the active sites on the cathode take part in the discharge process. Therefore, the optimal amount of electrolyte is essential toward air cathode performance. The unique triple-phase structure introduced by the textile-based cathode also results in a sufficient supply of oxygen and Li^+ ions during the discharge process, which leads to a much higher utilization of cathode active sites and improved discharge capacity. The breathable design also has positive effect on the charge potential, leading to a decrease of 0.1 V in charge potential (Figure S4, Supporting Information). The importance of the breathable cathode was also illustrated by studying the effect of the catalysts. With the breathable design, the battery without Pd catalyst also shows high capacity of 5.8 mAh cm^{-2}. However, due to the absence of catalysts, both the charge and discharge overpotentials are higher (Figure S5, Supporting Information). Moreover, due to the breathable architecture, the Li–O_2 battery also shows improved performance at elevated current densities, retaining a 4 mAh cm^{-2} capacity at 0.5 mA cm^{-2} (Figure S6, Supporting Information).

Beyond the full discharge condition, the rechargeability of the textile-based Li–O_2 cathode was also studied. The breathable cell was cycled with a charge/discharge capacity limit of 1 mAh cm^{-2} at a current density of 0.1 mA cm^{-2} (**Figure 5**a). In the first cycle, due to the activation process, the overall overpotential is 1.4 V; however, the cell began to stabilize in subsequent cycles with an overall overpotential of 1.15 V. Remarkably, the overpotential remained at 1.15 V even after 50 cycles without any obvious drop in performance (Figure 5b).

Characterization of the discharge products formed on the breathable textile-based air cathode confirmed the cell

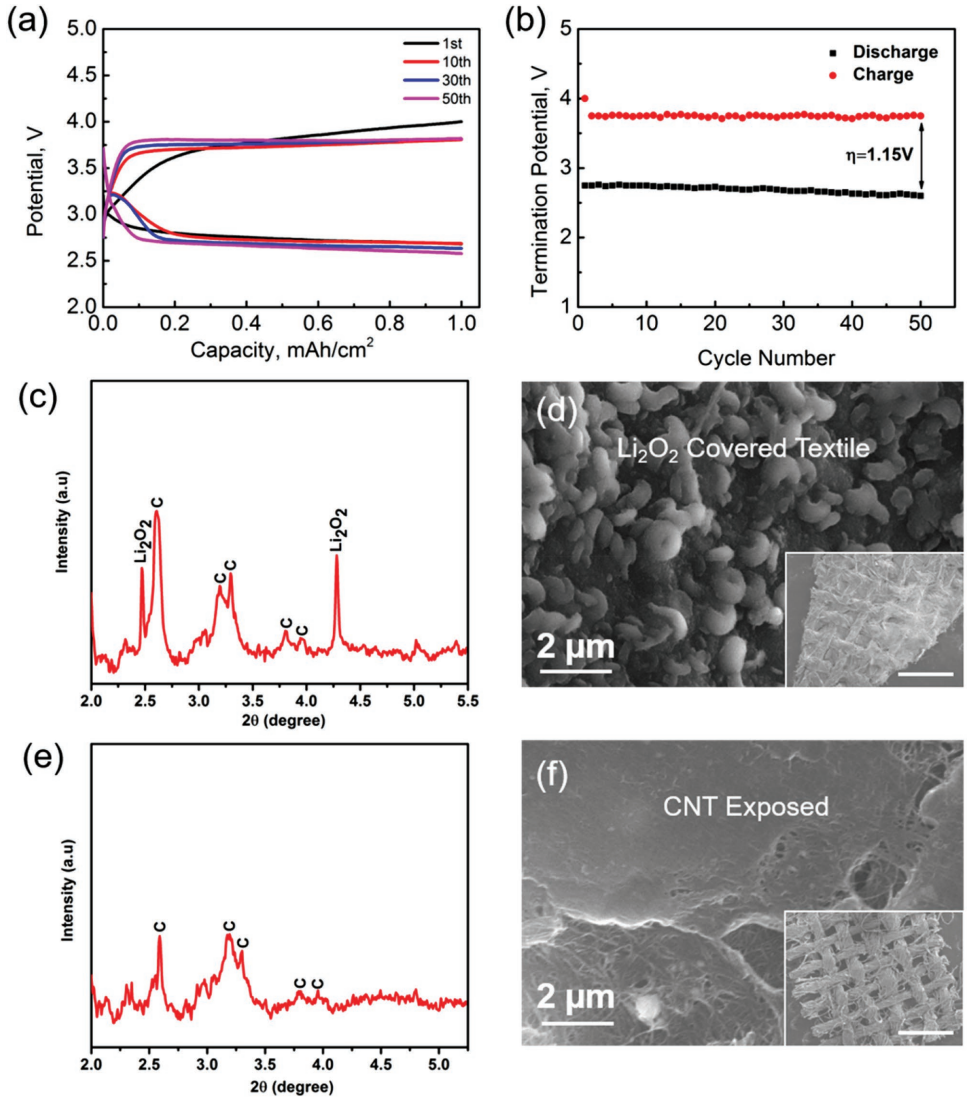

Figure 5. The rechargeability of the textile-based Li–O_2 cathode. a) Discharge/charge profile for the 50 cycles. No performance decay was observed and the overpotential remains constant at 1.15 V. b) The termination voltage of the charge/discharge processes for 50 complete cycles, where a low overpotential of 1.15 V is maintained. c) XRD spectrum of the breathable air cathode after discharge, where distinct Li_2O_2 peaks are observed. d) The SEM image of the air cathode in the discharge state shows toroid-shaped Li_2O_2. e) XRD spectrum of the textile-based air cathode in the charge state. The absence of Li_2O_2 peaks indicates the complete decomposition of the discharge product. f) SEM of the air cathode after charging. The layer of discharge products has vanished during the charge process to expose the CNT coating.

rechargeability (Figure 5c–f). The X-ray diffraction (XRD) results (Figure 5c) indicate the formation of lithium peroxide (Li_2O_2) occurs during the discharge process, which is consistent with previous reports.[21] Moreover, Raman spectroscopy and XPS were employed to analyze the specific discharge products. Figure S7a in the Supporting Information shows the Raman spectra for the breathable cathode in the discharge state with distinct Li_2O_2 peaks.[21] Note that in order to have sufficient discharge product for Raman spectrum, the battery was discharged to 2 V, leading to discharge of the ether-based electrolyte. Therefore, Li_2CO_3 peaks were observed from the Raman spectrum. The presence of Li_2O_2 is also observed in the discharged cathode via XPS. Specifically, the O 1s core peak shows a characteristic Li_2O_2 peak at 528 eV, which verifies the typical discharge product is formed on the textile-based air cathode (Figure S8a, Supporting Information).[41] When the cell is in the charge state, the XRD (Figure 5e), Raman (Figure S7b, Supporting Information) and XPS (Figure S8b, Supporting Information) results indicate the absence of Li_2O_2 on the textile-based cathode surface. Thus, the Li_2O_2 deposited during the discharge process is completely decomposed upon charging, which facilitates continued cyclability of the cathode without leftover insulating products. The morphology of the cathode after the charge/discharge was also determined by SEM. Figure 5d shows a dense layer of toroid Li_2O_2 covers the CNT-coated textile upon discharge, which is consistent with previous reports on Li_2O_2 deposition. Note that the textile mesh holes are completely filled with discharge products (Figure 5d inset), which indicates a solution-based mechanism for the formation of Li_2O_2.[8,21] When the cathode in the charge state, the CNT

layer becomes exposed and the toroid discharge product completely disappears (Figure 5f). Therefore, complete Li_2O_2 deposition-decomposition during the discharge/charge processes ensures the freshness of the cathode at each cycle and leads to stable cyclability (>50 cycles) for the textile-based Li–O_2 battery.

For the first time, we developed a flexible and high-performance lithium–air cathode composed of a breathable textile fabric. Unlike the conventional Li–O_2 battery cathode architecture, a unique triple-phase structure arises due to the wet textile fiber network (rapid electrolyte transport), the mesh holes formed by the woven fabric (oxygen diffusion) as well as the electronically conductive CNT coating layer. Since the electrolyte and oxygen gas have decoupled pathways, the active sites on the breathable CNT-coated cathode can be fully utilized for improved discharge performance (8.6 mAh cm^{-2}). Additionally, the loaded Pd nanocatalysts are easily accessible to both electrolyte and oxygen gas, which helps facilitate the ORR/OER processes and results in a low overpotential of 1.15 V after 50 cycles. The nature of the highly bendable and twistable textile-based cathode also promotes future flexible/wearable Li–O_2 battery design. The application of textile-based triple-phase structures is not limited in Li–O_2 battery. Other facilities involving reaction on multiple phase interlayer can also take advantage of the individual pathways for the liquid phase and the gas phase, such as the fuel cells, the electrocatalytical or photocatalytical water splitting, and the redox flow batteries.

Experimental Section

Fabrication of the Textile-Based Cathode: The textile-based cathode was fabricated by dip coating the textile fabric (65% polyester and 35% cotton) in a 10 mg mL^{-1} single-walled carbon nanotube (SWCNT, Carbon Solutions) dispersion repeatedly. After SWCNT coating, the textile was immersed in an aqueous 2 mg mL^{-1} $PdCl_2$ (Sigma-Aldrich) solution for 12 h to load the catalyst precursor. After the water evaporated, an aqueous $NaBH_4$ solution was dropped onto the textile to reduce the $PdCl_2$ salt to Pd nanoparticles. The fabricated cathode was then rinsed several times to remove any salt that remained.

Li–O_2 Cell Assembly and Testing: Li–O_2 battery assembly was completed in an argon-filled glovebox with O_2 and H_2O levels below 0.1 ppm using CR2032 type coin cells. Lithium metal was used as the anode and 1 M LiTFSI (Sigma-Aldrich) in tetraethylene glycol dimethyl ether (TEGDME) (Sigma-Aldrich) was used as the electrolyte. A glass fiber (Whatman) separator was used to physically separate the anode and the cathode. To fabricate the breathable cell, the separator and cathode were both immersed in the liquid electrolyte. The excess electrolyte was then carefully squeezed out of the separator and cathode to ensure an optimal amount of electrolyte (20 mg cm^{-2}) before cell assembly and crimping. To create the flooded control cell, the soaked separator and cathode with excess electrolyte were used directly in cell assembly (300 mg cm^{-2} electrolyte). The coin cell was then sealed in a custom-built chamber filled with oxygen gas (1 atm) and connected to the battery tester (Neware) for electrochemical testing.

Material Characterization: SEM images were captured with a Hitachi SU-70 field-emission gun (FEG) SEM. The XRD patterns were obtained with a Bruker D8 Advance system. Raman spectrum was obtained with a Yvon Jobin LabRam ARAMIS Raman spectrometer. XPS spectra were obtained using a high sensitivity Kratos AXIS 165 spectrometer. The ionic conductivity of the cathode was determined from EIS results tested on a BioLogic electrochemical workstation. The electronic conductivity was measured with a custom four-point probe apparatus using a Keithley DC power supply. The full textile consists of one piece with 2 cm × 2 cm dimensions. A single textile fiber is retrieved from the whole textile with a length of 5 cm and a diameter of 60 µm.

Postmortem Characterization of Li–O_2 Discharge and Charge Products: After cycling cells to the discharge/charge state, the samples were placed in an argon-filled glovebox before further characterization. Field emission scanning electron microscopy (FESEM) (Hitachi S4700) was used to characterize the morphology of the discharge and charge products. Samples were carefully transferred from the glovebox to the microscope chamber using argon-filled polybags to avoid exposure and unwarranted side reaction with ambient air. High-energy XRD was used to determine the phase structure of the discharge and charge products at the 11-ID-C beamline of the Advanced Photon Source, Argonne National Laboratory. The X-ray specimens were well-sealed with Kapton tape to protect against ambient air and then scanned at a wavelength of 0.1173 Å. The XRD profiles were collected by a Perkin-Elmer large area detector in transmission mode. Raman spectra of the discharge and charge products were obtained using an inVia Renishaw 2000 microscope spectrometer with an HeNe laser (633 nm wavelength). The samples were sealed in a gas-tight Raman sample holder with a glass window. Raman spectra were collected in 180° reflective mode with a collection time of 50–80 s.

Supporting Information

Supporting Information is available from the Wiley Online Library or from the author.

Acknowledgements

The authors acknowledge the support of the Maryland NanoCenter and its AIMLab as well as the facilities at Argonne National Laboratory. The team at Argonne National Laboratory was supported by the U.S. Department of Energy (DOE) under Contract DEAC0206CH11357 and the Vehicle Technologies Office, DOE, Office of Energy Efficiency and Renewable Energy (EERE). Use of the Advanced Photon Source and Center of Nano Materials, Office of Science User Facilities operated for the U.S. Department of Energy (DOE) Office of Science by Argonne National Laboratory, was supported by the U.S. DOE under Contract No. DE-AC02-06CH11357. S.D.L. acknowledges the support by the Department of Defense (DoD) through the National Defense Science and Engineering Graduate (NDSEG) Fellowship Program.

Conflict of Interest

The authors declare no conflict of interest.

Keywords

air cathode architecture, decoupled transport pathways, lithium–oxygen batteries, long cyclability, low overpotential

Received: August 27, 2017
Revised: September 25, 2017
Published online: December 8, 2017

[1] K. M. Abrahm, Z. Jiang, *J. Electrochem. Soc.* **1996**, *143*, 1.
[2] N. Feng, P. He, H. Zhou, *Adv. Energy Mater.* **2016**, *6*, 1502303.
[3] D. Geng, N. Ding, T. S. Andy Hor, S. W. Chien, Z. Liu, D. Wuu, X. Sun, Y. Zong, *Adv. Energy Mater.* **2016**, *6*, 1502164.
[4] L. Grande, E. Paillard, J. Hassoun, J. Park, Y. Lee, Y. Sun, S. Passerini, B. Scrosati, *Adv. Mater.* **2015**, *27*, 784.

[5] M. Balaish, A. Kraytsberg, Y. Ein-Eli, *Phys. Chem. Chem. Phys.* **2014**, *16*, 2801.
[6] G. Girishkumar, B. McCloskey, A. C. Luntz, S. Swanson, W. Wilcke, *J. Phys. Chem. Lett.* **2010**, *1*, 2193.
[7] P. Albertus, G. Girishkuar, B. McCloskey, R. S. Sanchez-Carrera, B. Kozinsky, J. Christensen, A. C. Luntz, *J. Electrochem. Soc.* **2011**, *158*, A343.
[8] S. Lau, L. A. Archer, *Nano Lett.* **2015**, *15*, 5995.
[9] S. A. Freunberger, Y. Chen, Z. Peng, J. M. Griffin, L. J. Hardwick, F. Barde, P. Novak, P. G. Bruce, *J. Am. Chem. Soc.* **2011**, *133*, 8040.
[10] S. A. Freunberger, Y. Chen, N. E. Drewett, L. J. Hardwick, F. Barde, P. G. Bruce, *Angew. Chem., Int. Ed.* **2011**, *50*, 8609.
[11] H. K. Lim, H. D. Lim, K. Y. Park, D. H. Seo, H. Gwon, J. Hong, W. A. Goddard, H. Kim, K. Kang, *J. Am. Chem. Soc.* **2013**, *135*, 9733.
[12] S. Xu, S. K. Das, L. A. Archer, *RSC Adv.* **2013**, *3*, 6656.
[13] P. Tan, Z. H. Wei, W. Shyy, T. S. Zhao, X. B. Zhu, *Energy Environ. Sci.* **2016**, *9*, 1783.
[14] X. B. Zhu, T. S. Zhao, Z. H. Wei, P. Tan, L. An, *Energy Environ. Sci.* **2015**, *8*, 3745.
[15] B. Zhou, L. Guo, Y. Zhang, J. Wang, L. Ma, W. Zhang, Z. Fu, Z. Peng, *Adv. Mater.* **2017**, *29*, 1701568.
[16] M. Asadi, B. Kumar, C. Liu, P. Phillips, P. Yasaei, A. Behranginia, P. Zapol, R. F. Klie, L. A. Curtiss, A. Salehi-Khojin, *ACS Nano* **2016**, *10*, 2167.
[17] J. Xu, Q. Liu, Y. Yu, J. Wang, J. Yan, X. Zhang, *Adv. Mater.* **2017**, *29*, 1606552.
[18] J. Shui, Y. Lin, J. W. Connell, J. Xu, X. Fan, L. Dai, *ACS Energy Lett.* **2016**, *1*, 260.
[19] Y. Lin, B. Moitoso, C. Martinez-Martinez, E. D. Walsh, S. D. Lacey, J. Kim, L. Dai, L. Hu, J. W. Connell, *Nano Lett.* **2017**, *17*, 3252.
[20] J. Xu, Z. Chang, Y. Wang, D. Liu, Y. Zhang, X. Zhang, *Adv. Mater.* **2016**, *28*, 9620.
[21] J. Lu, Y. J. Lee, X. Luo, K. C. Lau, M. Asadi, H. Wang, S. Brombosz, J. Wen, D. Zhai, Z. Chen, D. J. Miller, Y. S. Jeong, J. Park, Z. Z. Fang, B. Kumar, A. Salehi-Khojin, Y. Sun, L. A. Curtiss, K. Amine, *Nature* **2016**, *529*, 377.
[22] S. Xu, Q. Zhu, J. Long, H. Wang, X. Xie, K. Wang, J. Chen, *Adv. Funct. Mater.* **2016**, *26*, 1365.
[23] T. Liu, M. Leskes, W. Yu, A. J. Moore, L. Zhou, P. M. Bayley, G. Kim, C. P. Grey, *Science* **2015**, *350*, 530.
[24] Z. Zhu, A. Kushima, Z. Yin, L. Qi, K. Amine, J. Lu, J. Li, *Nat. Energy* **2016**, *1*, 16111.
[25] B. J. Bergner, A. Schürmann, K. Peppler, A. Garsuch, J. Janek, *J. Am. Chem. Soc.* **2014**, *136*, 15054.
[26] T. Zhang, K. Liao, P. He, H. Zhou, *Energy Environ. Sci.* **2016**, *9*, 1024.
[27] T. Zhang, H. Zhou, *Nat. Commun.* **2013**, *4*, 1817.
[28] S. Xu, S. Lau, L. A. Archer, *Inorg. Chem. Front.* **2015**, *2*, 1070.
[29] Z. Xie, X. Zhang, Z. Zhou, *Adv. Mater.* **2017**, *29*, 1605891.
[30] X. Hu, Z. Li, J. Chen, *Angew. Chem., Int. Ed.* **2017**, *56*, 5785.
[31] J. Jiang, H. Deng, X. Li, S. Tong, P. He, H. Zhou, *ACS Appl. Mater. Interfaces* **2016**, *8*, 10375.
[32] G. Zhou, F. Li, H. Cheng, *Energy Environ. Sci.* **2014**, *7*, 1307.
[33] X. Pu, L. Li, H. Song, C. Du, Z. Zhao, C. Jiang, G. Cao, W. Hu, Z. L. Wang, *Adv. Mater.* **2015**, *27*, 2472.
[34] Y. Zhang, L. Wang, Z. Guo, Y. Xu, Y. Wang, H. Peng, *Angew. Chem., Int. Ed.* **2016**, *55*, 4487.
[35] Q. Liu, J. Xu, D. Xu, X. Zhang, *Nat. Commun.* **2015**, *6*, 7892.
[36] Q. Liu, L. Li, J. Xu, Z. Chang, D. Xu, Y. Yin, X. Yang, T. Liu, Y. Jiang, J. Yan, X. Zhang, *Adv. Mater.* **2015**, *27*, 8095.
[37] Q. Liu, T. Liu, D. Liu, Z. Li, X. Zhang, Y. Zhang, *Adv. Mater.* **2016**, *28*, 8413.
[38] T. Liu, Q. Liu, J. Xu, X. Zhang, *Small* **2016**, *12*, 3101.
[39] D. Shou, Y. Tang, L. Ye, J. Fan, F. Ding, *Int. J. Hydrogen Energy* **2013**, *38*, 10519.
[40] J. P. Feser, A. K. Prasad, S. G. Advani, *J. Power Sources* **2006**, *162*, 1226.
[41] Y. Lu, E. J. Crumlin, G. M. Veith, J. R. Harding, E. Mutoro, L. Baggetto, N. J. Dudney, Z. Liu, Y. Shao-Horn, *Sci. Rep.* **2012**, *2*, 715.